Fluid Dynamics & Materials Processing

Tech Science Press

DOI: 10.32604/fdmp.2024.051506

ARTICLE

The Influence of CO_2 Cured Manganese Slag on the Performance and Mechanical Properties of Ultra-High Performance Concrete

Ligai Bai and Guihua Yang*

School of Architectural Engineering, North China Institute of Aerospace Engineering, Langfang, 065000, China

*Corresponding Author: Guihua Yang. Email: jiangong3201@nciae.edu.cn

Received: 06 March 2024 Accepted: 16 June 2024 Published: 06 August 2024

ABSTRACT

The presence of toxic elements in manganese slag (MSG) poses a threat to the environment due to potential pollution. Utilizing CO_2 curing on MS offers a promising approach to immobilize toxic substances within this material, thereby mitigating their release into the natural surroundings. This study investigates the impact of CO_2 cured MS on various rheological parameters, including slump flow, plastic viscosity (η), and yield shear stress (τ). Additionally, it assesses flexural and compressive strengths (f_t and f_{cu}), drying shrinkage rates (DSR), durability indicators (chloride ion migration coefficient (CMC), carbonization depth (CD)), and the leaching behavior of heavy metal elements. Microscopic examination via scanning electron microscopy (SEM) is employed to elucidate the underlying mechanisms. The results indicate that CO_2 curing significantly enhances the slump flow of ultra-high performance concrete (UHPC) by up to 51.2%. Moreover, it reduces UHPC's η and τ by rates ranging from 0% to 52.7% and 0% to 40.2%, respectively. The DSR exhibits a linear increase corresponding to the mass ratio of CO_2 cured MS. Furthermore, CO_2 curing enhances both f_t and f_{cu} of UHPC by up to 28.7% and 17.6%, respectively. The electrical resistance is also improved, showing an increase of up to 53.7%. The relationship between mechanical strengths and electrical resistance follows a cubic relationship. The CO_2 cured MS demonstrates a notable decrease in the CMC and CD by rates ranging from 0% to 52.6% and 0% to 26.1%, respectively. The reductions of leached chromium (Cr) and manganese (Mn) are up to 576.3% and 1312.7%, respectively. Overall, CO_2 curing also enhances the compactness of UHPC, thereby demonstrating its potential to improve both mechanical and durability properties.

KEYWORDS

CO_2 curing; manganese slag; steel fibers; mechanical strengths; salt action

1 Introduction

Electrolytic manganese slag (MS) represents a significant solid waste byproduct, with a notable annual output [1,2]. In its untreated state, MS contains heavy metal ions such as Mn^{2+} and NH^{4+}, which may leach into the environment and contribute to soil and water contamination, thereby presenting significant environmental hazards [3,4]. Conventional methods present challenges in efficiently and economically removing manganese ions (Mn^{2+}) and ammonium ions (NH^{4+}) concurrently. Consequently, there is a pressing necessity for the development of novel methodologies for the treatment of MS.

In civil engineering applications, cement stands as the predominant material [5,6]. The active components within MS have been enhanced to strengthen both the mechanical characteristics and cement matrix's durability [7]. Incorporating solid wastes into cement can both immobilize harmful substances and enhance the performance of cement-based materials concurrently [8]. A number of waste materials, including fly ash, furnace ash, secondary aluminum ash, steel slag, and others, have been demonstrated to enhance the mechanical properties and durability of cement matrices [9,10]. However, ordinary cement-based materials typically possess large pores, which facilitate the leaching of toxic substances from solid wastes. Consequently, cement-based materials with high compactness are required to effectively solidify these wastes [11,12]. A substantial body of academic research has investigated the potential of ultra-high performance concrete (UHPC) as a consolidating agent for solid waste materials [13,14].

UHPC represents a novel cement-based material that has been developed through the application of high-density theory. This innovative approach results in the creation of a highly robust, compact substance [15,16]. The incorporation of fly ash, furnace ash, and secondary aluminum ash into UHPC has been demonstrated to enhance both flexural and compressive strengths by up to 23.6% and 31.1%, respectively [17,18]. Furthermore, the incorporation of active solid waste into UHPC results in a reduction of the chloride ion migration coefficient, carbonization depth, and susceptibility to freeze-thaw damage [19,20]. Moreover, the solidification of solid waste within UHPC significantly minimizes the release of toxic substances, as evidenced by studies [21,22].

The application of CO_2 curing, a recent technique in treating hazardous solid waste ash, has demonstrated efficacy in preventing the escape of harmful substances [23]. Moreover, when implemented on solid waste ash, CO_2 curing concurrently enhances the cement matrix's mechanical strength and durability [24,25]. The incorporation of CO_2 cured waste fly ash results in a notable increase of 31.2% and 28.7% in flexural and compressive strengths of UHPC, respectively. Similarly, utilizing CO_2 cured stove ash leads to enhancements of 27.1% and 22.4% in flexural and compressive strengths, respectively [26,27]. CO_2 curing additionally enhances the resistance of UHPC to chloride penetration, chloride freeze-thaw, and chloride corrosion by improving its compactness [28,29]. The implementation of CO_2 curing holds promise in reducing toxic substances within MS and consolidating toxins, which could potentially enhance the mechanical properties of the cement matrix containing MS, representing a promising avenue for research innovation [30,31]. However, there is a scarcity of research reports focusing on this aspect.

The impact of CO_2 cured manganese slag (MSG) on the flexural and compressive strengths and drying shrinkage rate (DSR) of ultra-high performance concrete (UHPC) were explored in this study. Meanwhile, the chloride ion permeability and carbonization resistance were investigated. Furthermore, the leached Mn and Cr were measured. The scanning electron microscope (SEM) were assessed to analyze macroscopic performance mechanisms. The objective of these findings was to propose innovative approaches for the treatment of MSG.

2 Materials and Methods

2.1 Raw Materials

The following binding materials were utilized in this study: fly ash (FA), manganese slag (MSG), and ordinary Portland cement (OPC). The FA and OPC were procured from Tianjin Shengsanyang Chemical Trading Co., Ltd., Tianjin, China, while the MSG was sourced from Dongguan Runze Building Materials Co., Ltd., Dongguan, China. The initial setting time and final setting time of OPC were 103.1 and 217.4 min, showing the strength grade of 42.5 MPa. The densities of FA, OPC and MS were 1.36, 3.15, and 3.01 g/cm^3, respectively. Quartz sand (QZS) whose particle sizes were 0.01~1 mm, continuous grading, sourced from Sichuan Yishi Stone Co., Ltd., Chengdu, China, was used as the aggregate. The

chemical composition and particle size distribution chemical composition and particle size distribution of the raw materials are shown in Tables 1 and 2.

Table 1: The accumulated pass rate (%)

Types	Particle size/μm						
	0.3	0.6	1	4	8	64	360
OPC	0.11	0.36	3.07	14.75	29.12	92.63	100
FA	12.2	41.6	66.1	93.8	100	100	100
QZS	0	0	0	0	0.038	24.01	100
MSG	0.07	0.31	1.38	8.75	23.51	98.45	100

Table 2: Chemical constituents (%)

Types	SiO_2	Al_2O_3	Fe_xO_y	MgO	CaO	SO_3	K_2O	MnO_2	Loss on ignition
OPC	20.3	5.6	3.9	1.7	62.4	2.8	–	–	3.0
FA	54.00	21.00	5.00	11.20	4.40	0.21	1.23	2.15	0.07
QZS	98.3	–	1.5	–	–	–	–	–	–
MSG	34.21	7.33	12.04	1.90	13.91	0.07		30.55	–

2.2 The Preparing of Samples

The UHPC's manufacturing process for the is outlined below. Firstly, all the dry materials were poured into the UJZ-15 Vertical Mortar Mixer, offered by Xian County Xusheng Construction Testing Instrument Co., Ltd., Xi'an, China. One minute's stirring with the speed of 140 r/min was conducted. After that the water and water reducing agent were provided and 5 min' mixing by the same speed were finished. Table 3 demonstrates the UHPC's mixing proportions.

Table 3: The UHPC's mixing proportions (kg/m^3)

Water	OPC	MSG	SF	QZS	HRWR
244.8	671.2	0	186.7	981.2	16.3
244.8	578.3	92.8	186.7	981.2	16.3
244.8	486.5	184.6	186.7	981.2	16.3
244.8	390.7	279.5	186.7	981.2	16.3
244.8	298.9	372.3	186.7	981.2	16.3

2.3 Experimental Methodology

2.3.1 The Rheological Parameters' Measuring Process

The slump flow of fresh UHPC is determined using the NLD-3 cement mortar flowability tester from Shanghai Meiyu Instrument Technology Co., Ltd., Shanghai, China, following the Jumping table method

specified in GB/T 50080-2016 [32]. The Brookfield DVNext Rheometer is used for the yield shear stress (τ) and plastic viscosity (η)'s measurement. The rotation speed of the Rheometer ranges from 0.1~1.3 × 10^5 Pa·s. The measurement of η and τ is carried out according to the Chinese standards GB/T 2794-2022 and GB/T 7124-2008 [33,34].

2.3.2 The Measurement of UHPC's Initial Setting Time

Cangzhou Lucheng Engineering Instrument Co., Ltd., Cangzhou, China's ZKS-100 pointer type cement mortar setting time tester is used for testing the initial setting time. The inner diameter and depth of trial mold are 140 and 75 mm. Test needle cross-sectional area is 30 mm^2.

2.3.3 The Measurement of UHPC's Drying Shrinkage Rate

The specimens with sizes of 40 mm × 40 mm × 160 mm are installed on fixed bracket. The micrometer caliper is used for testing the dry shrinkage length. Additionally, the Eq. (1) is used for calculating the drying shrinkage rate (S_d).

$$S_d = \frac{L_t - L_0}{L_0} \tag{1}$$

L_0 and L_t are the initial length and the length during the curing ages, respectively.

2.3.4 The Measurement of Mechanical Parameters

A fully automated bending integrated testing machine is used to determine the flexural and compressive strengths, applying loading rates of 0.05 and 2.4 kN/s, respectively. The testing of mechanical strengths for UHPC specimens follows the Chinese standard GB/T 17671-2005 [35]. All samples are cured at 20°C ± 1°C temperature and above 98% relative humidity.

2.3.5 The Electrical Resistance's Measuring Process

The AC electrical resistance is measured using the Tonghui TH2832 high-performance compact precision LCR digital bridge, sourced from Shenzhen Shijia Instrument Co., Ltd., Shenzhen, China. Electrical voltage (1 V), testing frequency (10^5 Hz), and sampling frequency (10^5 Hz) are meticulously set. Cube samples with a side length of 50 mm are specifically chosen for electrical resistance measurement, with two embedded electrodes facilitating the application of AC voltage.

2.3.6 The Determination of Chloride Ion Permeability and Carbonation

The chloride migration coefficient (CMC) in concrete is assessed through non-steady-state migration tests, which involve applying a voltage gradient across a concrete specimen. The movement of chloride ions over time is precisely measured using the rapid chloride migration (RCM) method.

Concrete carbonation depth is typically assessed using phenolphthalein solution. This procedure entails spraying the solution onto a freshly fractured concrete surface and carefully observing color changes. The transition from pink to colorless indicates the depth of carbonation. Alternatively, concrete cores can be extracted and analyzed using the indicator titration method. The measurements of the CMC and the carbonation depth are carried out by Chinese standard GB/T 50082-2009 [36].

2.3.7 The Micro-Properties' Measuring Process

Scanning electron microscope (SEM) experiments are conducted using dried samples of flat, rice-sized portions extracted from the specimens. Subsequently, the samples are metallized with gold before being placed in a vacuum environment for observation. In this study, the Nova Nano SEM scanning electron microscope is utilized to examine the microstructure. It boasts a resolution of 3.5 nm, an acceleration voltage ranging from 500 to 30000 V, a magnification range of 18 to 30000, and a sample stage diameter of 30 mm. The experimental process is depicted in Fig. 1.

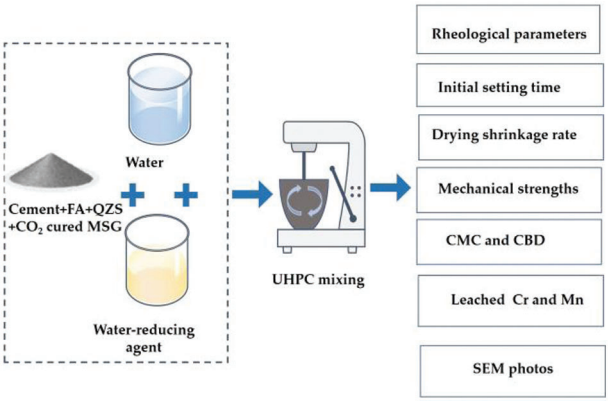

Figure 1: The process of the experiments

3 Results and Discussions

3.1 The UHPC's Rheological Parameters

Fig. 2 demonstrates the fresh UHPC's slump flow (*S*) with different dosages of CO_2 cured MSG. The *S* is determined after the stirring of fresh UHPC is finished for 0, 0.5 and 1 h. It can be found in Fig. 2, the *S* shows a positive trend with the CO_2 cured MSG, due to the fact that the CO_2 curing on MSG can reduce the internal pores of MSG [37]. Therefore, the MSG adsorbs less free water, hence, the fluidity of UHPC increases with the added CO_2 cured MSG. While, the *S* shows negative trend by the standing time. The results can be interpreted as the free water being evaporated during the placed time [38]. Consequently, the *S* decreases with the placing time. The increasing rates of *S* by CO_2 cured MSG range from 0% to 51.2%. While, the decreasing rates of *S* by the placing time are 0%~43.2%. The error bars are lower than 7.3% of the *S*'s real values, showing the measuring accuracy.

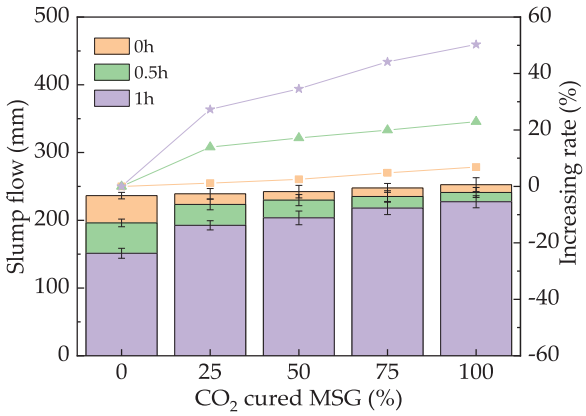

Figure 2: The *S* of fresh UHPC with CO_2 cured MSG

Fig. 3 displays the fresh UHPC' η. As exhibited in Fig. 3, the η decreases (decreasing rates of 0%~52.7%) by adding the CO_2 cured MSG, which is related to the reduced pores by CO_2 curing on MSG, leading to a lower content of free water [39]. However, when the placing time of fresh UHPC increases from 0 to 1 h, the fresh UHPC shows ascending trend with the placing time. The error bars' values are lower than 6.7% of the η's real values, ensuring the experimental correctness.

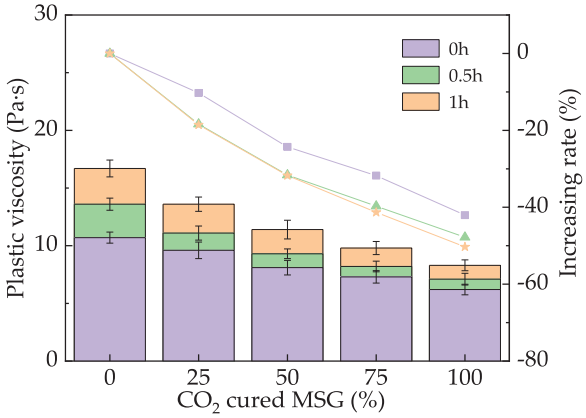

Figure 3: The fresh UHPC's η with CO_2 cured MSG

The τ of fresh UHPC is depicted in Fig. 4. It is evident from the graph that the τ of fresh UHPC follows a similar trend. The increasing CO_2 cured MSG leads to a reduction in the τ of fresh UHPC by 0% to 40.2%. This outcome is in alignment with the findings concerning τ. The primary rationale behind this observation lies in the optimization of chemical reactions and particle size distribution. On one hand, CO_2 reacts with calcium ions in concrete, yielding calcium carbonate that fills voids and enhances the microstructure. On the other hand, the fine calcium carbonate particles contribute to a filling effect, resulting in a more uniform particle size distribution within the concrete. The error bars in the figure denote experimental precision, with all values below 7.2% relative to the fresh UHPC's τ, underscoring the accuracy of the experimental results.

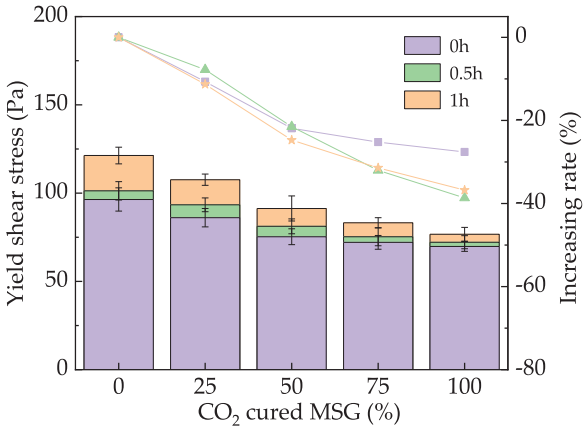

Figure 4: The τ of fresh UHPC with CO_2 cured MSG

3.2 The Initial Setting Time of UHPC

The initial setting time of UHPC is depicted in Fig. 5. The incorporation of CO_2 cured MSG extends the initial setting time of UHPC, with rates ranging from 0% to 16.3%. This delay is attributed to a reduction in the amount of free water due to CO_2 curing, which in turn prolongs the setting time. Moreover, the reaction between CO_2 and MSG may yield compounds distinct from calcium carbonate, potentially exhibiting different hardening properties and reaction rates. Consequently, this reaction could proceed at a slower pace, thereby prolonging the initial setting time [40]. The error bars associated with the initial setting time are less than 8.1% of the actual setting time values, ensuring the accuracy of the measurements.

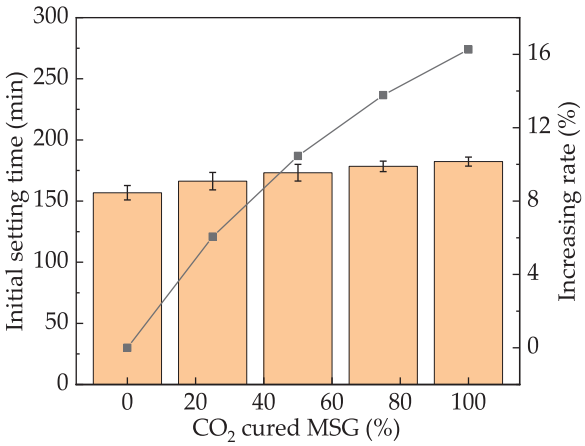

Figure 5: The initial setting time of UHPC with CO_2 cured MSG

3.3 The UHPC's DSR

The DSR of UHPC is provided in Fig. 6. It is observed that the UHPC's DSR demonstrates positive trend with the added CO_2 cured MSG, due to the secondary hydration effect of carbonization products of MS. Moreover, the curing age leads to increasing the DSR, due to the improved hydration degree. Hence, the free water is consumed by the improved hydration, leading to the increased DSR. In addition, the calcium carbonate produced by CO_2 curing on MSG may have different thermal expansion and contraction characteristics than the original cement matrix. This difference can cause internal stresses during the drying and hardening of concrete, which can increase drying shrinkage [41]. It can be found that the error bars are lower than 8.1% to the DSR.

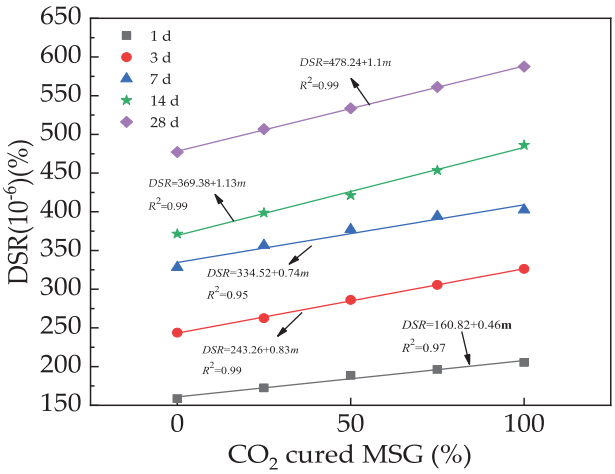

Figure 6: The DSR of UHPC with CO_2 cured MSG

3.4 The Mechanical Strengths of UHPC

The UHPC's f_t and f_{cu} are depicted in Fig. 7. As revealed in Fig. 7, the f_t and f_{cu} of UHPC ascend with the added CO_2 cured MSG by the rates of 0%~28.7% and 0%~17.6%, respectively. This is because the CO_2 curing on MSG can reduce the porosity of MSG to reduce the internal defects of UHPC thus improving its mechanical strengths. Moreover, the CO_2 curing on MSG can improve the secondary hydration of UHPC, leading to improving the mechanical strength. Furthermore, through CO_2 curing on MSG, the

resulting calcium carbonate particles play a crucial role in enhancing the interfacial adhesion between the cement matrix and the aggregate. These particles also serve to bridge and seal the microcracks formed during the initial stages, effectively halting the propagation of cracks. This mechanism significantly contributes to the increase in the strength and stability of the concrete [42]. The mechanical strengths show the error bars' values of lower than 7.3%, ensuring the testing precision.

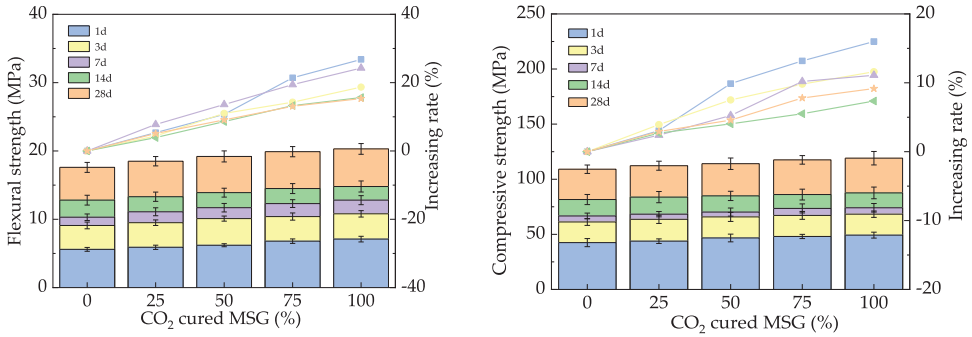

(a) Flexural strength (b) Compressive strength

Figure 7: The mechanical strengths of UHPC with CO_2 cured MSG

3.5 The Electrical Resistance of UHPC

Fig. 8 shows the variation of electrical resistance (R) with the mass ratios of CO_2 cured MSG. As observed in Fig. 8, R increases with the increasing dosages of CO_2 cured MSG. This can be explained by the carbonization effect on MSG, which solidifies the free ions within MSG. Furthermore, the presence of calcium carbonate particles fills the original pores and gaps, thereby reducing the interconnected pores within the concrete. The reduction in porosity implies fewer channels through which current can flow, leading to an overall increase in resistance [43]. Consequently, the electrical conductivity increases due to the CO_2 cured MSG. As observed, R rises from 0% to 57.3% as cured for 1~28 days. This is attributed to the enhanced degree of hydration over time, which reduces the amount of free water in the pore solution [44]. Therefore, the R of UHPC decreases with increased curing time. The error bars for R are less than 6.7% of the actual values, ensuring accuracy.

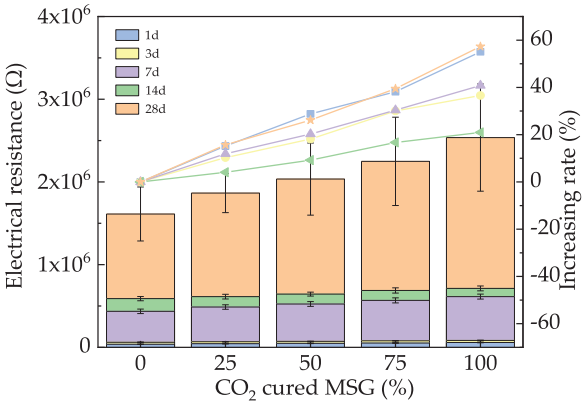

Figure 8: The R of UHPC with CO_2 cured MSG

The relationship between R and mechanical strengths is illustrated in Fig. 9. As shown, the mechanical strengths of UHPC and the corresponding R exhibit a cubic function relationship. This can be explained by the fact that the mechanical strengths of UHPC are closely related to its pore structure. The increased compactness of UHPC results in a denser concrete structure, reducing the migration of water and ions within the material. This reduction is crucial for enhancing R. Simultaneously, the decreased moisture and ionic permeability enable the concrete to better retain its structural integrity and load-bearing capacity under various loading conditions, thereby augmenting its mechanical strength [45]. While, the R of UHPC depends on UHPC's pore solution. The R of UHPC is closely related to the corresponding mechanical strengths.

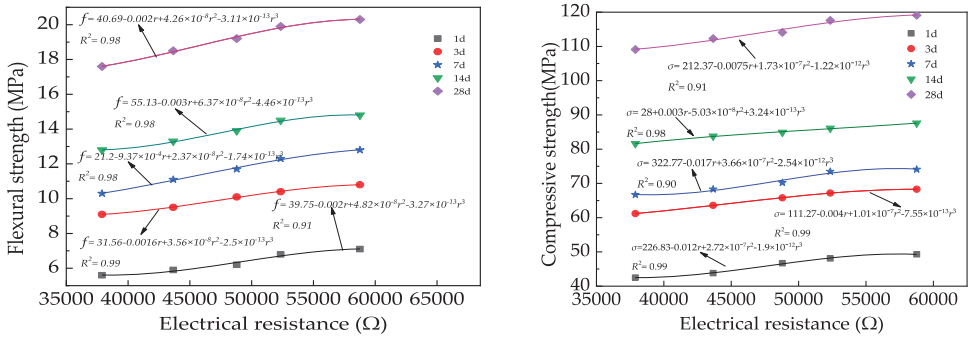

(a) The f_t and the R's fitting curves (b) The f_{cu} and the R's fitting curves

Figure 9: The fitting curves of R and the mechanical strengths of UHPC with CO_2 cured MSG

3.6 The CMC and CBD of UHPC

Fig. 10 shows the CMC of UHPC with different dosages of CO_2 cured MSG. As depicted, the CMC of UHPC exhibits a decrease with increasing dosages of CO_2 cured MSG, with decreasing rates ranging from 0% to 52.6%. This phenomenon can be attributed to the reduction in pores within the MSG and the enhanced secondary hydration facilitated by CO_2 curing. Additionally, the formation of calcium carbonate enhances the chemical stability of concrete. The high stability of calcium carbonate enables the formation of a durable protective layer in concrete, aiding in resistance against chloride ion erosion and penetration. Consequently, the chloride ion permeability of UHPC is diminished by the presence of CO_2 cured MS [46]. This results in an improvement in the compactness of UHPC upon the addition of CO_2 cured MS. The error bars associated with the CMC values are consistently below 7.3% of the total CMC, affirming the accuracy of the measurements.

The CBD of UHPC with varying mass ratios of CO_2 cured MSG is shown in Fig. 11. The CBD of UHPC exhibits a decreasing trend as the dosage of CO_2 cured MSG increases, with reductions ranging from 0% to 26.1%. This is attributed to the improved compactness [47]. Consequently, the migration efficiency of CO_2 in UHPC is limited, leading to a reduced CBD. The error bars for CBD are below 5.6%, indicating the experimental accuracy.

3.7 The Leached Toxic Heavy Metal Elements

Fig. 12 illustrates the leaching of Cr and Mn from the UHPC. As shown, the amounts of leached Cr and Mn decrease by 0% to 576.3% with increased dosages of CO_2 cured MS, but they increase by 0% to 1312.7% with longer immersion times. The CO_2 curing process promotes the formation of $CaCO_3$, which reduces the porosity in MSG. Calcium carbonate can chemically bind or adsorb heavy metal ions, immobilizing them in the solid phase and thereby decreasing their solubility and mobility in water [48]. Consequently, CO_2 curing on MSG leads to a decrease in the immersion of Cr and Mn. The immersion levels of Cr and Mn increase

with immersion time, reflecting the presence of pores in the UHPC. Notably, the amount of Cr immersed exceeds that of Mn. The error bars for the immersion of toxic heavy metal elements are within 7.3% of the actual amounts of Cr and Mn, affirming the accuracy of the experiments.

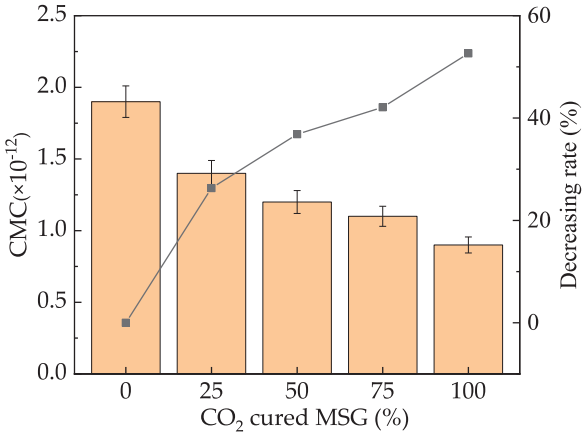

Figure 10: The CMC of UHPC with CO_2 cured MSG

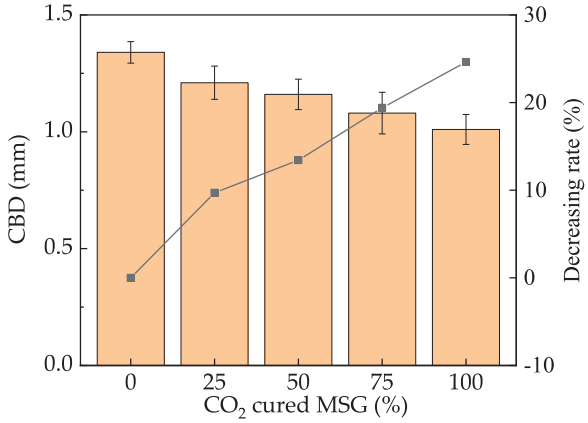

Figure 11: The CBD of UHPC with CO_2 cured MSG

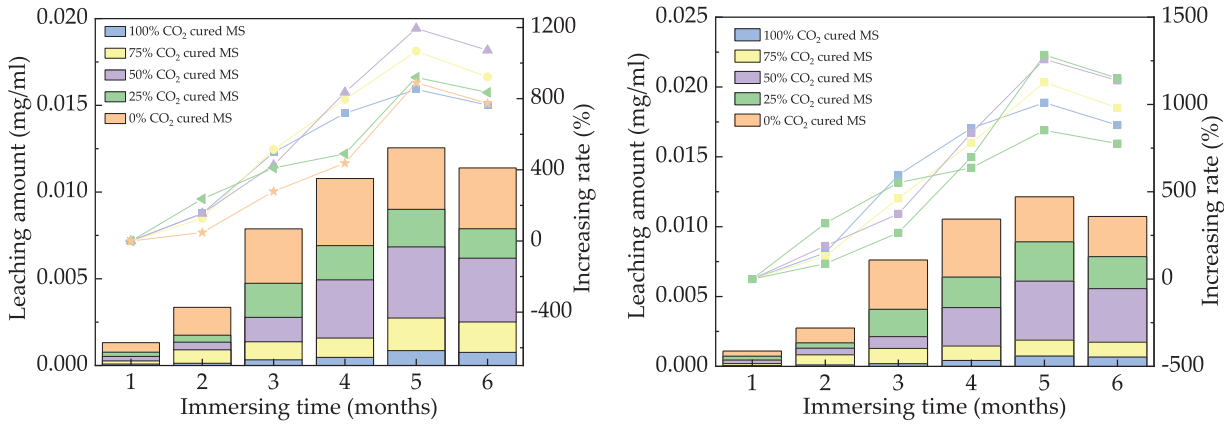

Figure 12: The leached Cr and Mn of UHPC with CO_2 cured MSG

3.8 The Microscopic Researching Results

The UHPC's SEM photos are provided in Fig. 13. The mass ratios of CO_2 cured MSG are 0%, 50% and 100%. The clustered hydration products and blocky hydration products are found in Fig. 13. While the hydrates become more compact after the CO_2 cured MSG is added, which is attributed to the formed carbonate by the CO_2 curing on MSG. Furthermore, CO_2 cured MSG enhances the integrity of the hydration reaction. The CO_2 curing process may facilitate more complete hydration of certain cement components by altering the local environment of the cement paste, including pH and ion concentration. This alteration contributes to the promotion of other cement hydration products' formation.

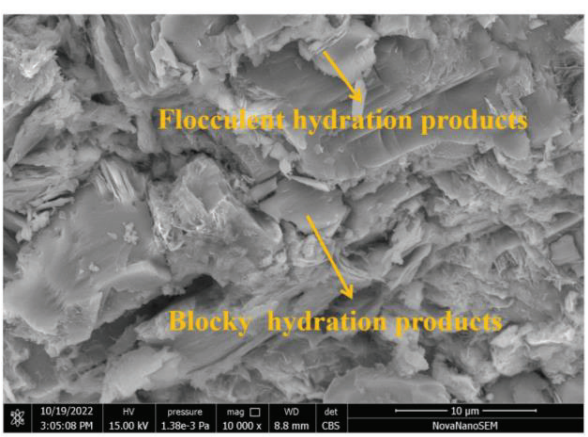

(a) With 0% CO_2 cured MSG

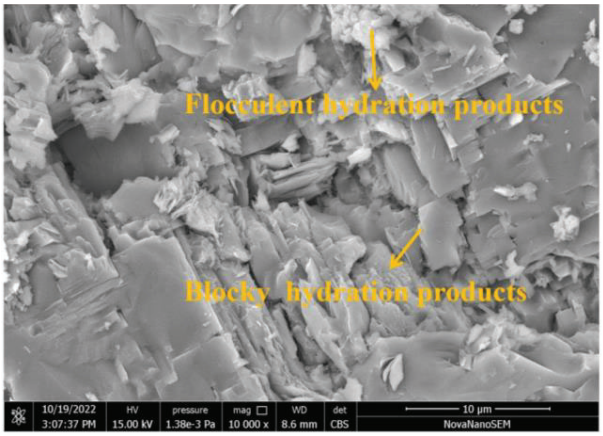

(b) With 50% CO_2 cured MSG

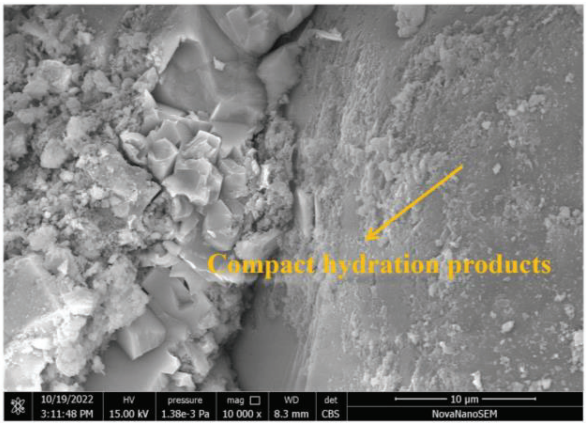

(c) With 50% CO_2 cured MSG

Figure 13: The SEM photos of UHPC with CO_2 cured MSG

4 Conclusions

The conclusions of this study are summarized as follows:

The incorporation of CO_2 cured MSG results in an elevation of the fresh UHPC's slump flow by rates of 0%~51.2%. Conversely, the corresponding plastic viscosity and yield shear stress of fresh UHPC decrease, with rates ranging from 0% to 52.7% and 0% to 40.2%, respectively.

CO_2 cured MS exhibits a retarding effect on UHPC by prolonging the initial setting time, with rates of 0% to 16.3%. This increase in initial setting time is accompanied by a corresponding rise in drying shrinkage rate.

The flexural and compressive strengths exhibit a decrease by rates of 0%~28.7% and 0%~17.6%, respectively, when the CO_2 cured MSG is added. Conversely, the electrical resistances of UHPC demonstrate an increasing trend with the CO_2 cured MSG's mass ratio by rates of 0%~57.3%. Notably, the mechanical strengths display a cubic function in relation to the electrical resistance of UHPC.

The chloride migration coefficient, carbonation depth, and leached Cr and Zn decrease with the added CO_2 cured MSG, with decreasing rates of 0%~52.6%, 0%~26.1%, 0%~576.3%, and 0%~1312.7%, respectively. This suggests that CO_2 cured MS effectively enhances the compactness of UHPC.

The research of the influence of CO_2 cured MSG on the UHPC's performance and mechanical properties can provide a reference for solving the accumulation and pollution of MSG. At the same time, this study can also offer a source of cementitious materials for the preparation of cementitious materials. However, multiple microscopic methods should be studied in the future to further analyze the mechanism of MSG affecting cement-based materials.

Acknowledgement: None.

Funding Statement: This research is supported by Hebei Province Higher Education Science and Technology Research Project (No. ZC2024031).

Author Contributions: Conceptualization, methodology, validation and formal analysis; Ligai Bai and Guihua Yang; investigation, writing—original draft preparation, resources, data curation, writing—review and editing; Ligai Bai; visualization, supervision, project administration, funding acquisition, Guihua Yang. All authors reviewed the results and approved the final version of the manuscript.

Availability of Data and Materials: The data that support this study are available from the corresponding authors upon reasonable request.

Conflicts of Interest: The authors declare that they have no conflicts of interest to report regarding the present study.

References

1. Kudyba A, Akhtar S, Johansen I, Safarian J. Aluminothermic reduction of manganese oxide from selected MnO-containing slags. Materials. 2021;14(2):356. doi:10.3390/ma14020356.
2. Gómez-Casero M, Bueno-Rodríguez S, Castro E, Quesada D. Alkaline activated cements obtained from ferrous and non-ferrous slags. Electric arc furnace slag, ladle furnace slag, copper slag and silico-manganese slag. Cem Concr Compos. 2024;147:105427. doi:10.1016/j.cemconcomp.2023.105427.
3. Cota T, Cheloni L, Guedes J, Reis É. Silico-manganese slag and its utilization into alkali-activated materials: a critical review. Constr Build Mater. 2023;399:132589. doi:10.1016/j.conbuildmat.2023.132589.
4. Toro N, Rodríguez F, Rojas A, Robles P, Ghorbani Y. Leaching manganese nodules with iron-reducing agents–a critical review. Miner Eng. 2021;163:106748. doi:10.1016/j.mineng.2020.106748.
5. Luther GW, AubinThibault TDCD, Oldham VE, Estes ER, Tebo BM, Madison AS. Reduction of manganese oxides: thermodynamic, kinetic and mechanistic considerations for one-versus twoelectron transfer steps. Aquat Geochem. 2018;24:257–77. doi:10.1007/s10498-018-9342-1.
6. Liu M, Dai W, Zhong C, Yang X. Study on mechanical properties and microstructure of manufactured sand reactive powder concrete with different curing methods. Mater Lett. 2023;335:133818. doi:10.1016/j.matlet.2023.133818.
7. Sharba AA. The efficiency of steel slag and recycled concrete aggregate on the strength properties of concrete. KSCE J Civ Eng. 2019;23(11):4846–51. doi:10.1007/s12205-019-0700-3.
8. Liu B, Meng H, Pan G, Zhou H. Relationship between the fineness and specific surface area of iron tailing powder and its effect on compressive strength and drying shrinkage of cement composites. Constr Build Mater. 2020;357(1):129421. doi:10.1016/j.conbuildmat.2022.129421.

9. Butkute K, Vaitkevicius V, Sinka M, Augonis A, Korjakins A. Influence of carbonated bottom slag granules in 3D concrete printing. Materials. 2023;16(11):4045. doi:10.3390/ma16114045.
10. Alderete N, Joseph A, Van den Heede P, Matthys S, De Belie N. Effective and sustainable use of municipal solid waste incineration bottom ash in concrete regarding strength and durability. Resour Conserv Recycl. 2021;167:105356. doi:10.1016/j.resconrec.2020.105356.
11. Mandpe A, Yadav N, Paliya S, Tyagi L, Yadav B, Singh L, et al. Exploring the synergic effect of fly ash and garbage enzymes on biotransformation of organic wastes in in-vessel composting system. Bioresour Technol. 2021;322(6):124557. doi:10.1016/j.biortech.2020.124557.
12. Saxena R, Gupta T, Sharma RK, Panwar NL. Influence of granite waste on mechanical and durability properties of fly ash-based geopolymer concrete. Environ Dev Sustain. 2021;23(12):17810–34. doi:10.1007/s10668-021-01414-z.
13. Cui L, Wang H. Influence of waste fly ash on the rheological properties of fresh cement paste and the following electrical performances and mechanical strengths of hardened specimens. Coatings. 2021;11:1558. doi:10.3390/coatings11121558.
14. Du Y, Hao W, Shi F, Wang H, Xu F, Du T. Investigations of the mechanical properties and durability of reactive powder concrete containing waste fly ash. Buildings. 2022;12(5):560. doi:10.3390/buildings12050560.
15. Xu W, Wang H, Tian X. The effect of secondary aluminum ash on the properties of reactive powder concrete. Materials. 2023;16(15):5265. doi:10.3390/ma16155265.
16. Mayhoub O, Nasr E, Ali Y, Kohail M. The influence of ingredients on the properties of reactive powder concrete: a review. Ain Shams Eng J. 2021;12:145–58. doi:10.1016/j.asej.2020.07.016.
17. Hang T, Luca S, David B. Development of sustainable ultra-high performance concrete recycling aluminum production waste. Constr Build Mater. 2023;371:130212. doi:10.1016/j.conbuildmat.2022.130212.
18. Yoo D, Banthia N, Lee J, Young-Soo Y. Effect of fiber geometric property on rate dependent flexural behavior of ultra-high-performance cementitious composite. Cem Concr Compos. 2018;86:57–71. doi:10.1016/j.cemconcomp.2017.11.002.
19. Liang Z, Peng X, Wang H. The influence of aspect ratio of steel fibers on the conductive and mechanical properties of compound cement reactive powder concrete. Coatings. 2023;13(2):2174738.
20. Ramesh Kumar G, Bharani S, Anupriya R, Jeevitha V, Gnanajothi G. Influence of electronic waste and fly ash in strength and durability properties of concrete. Mater Today: Proc. 2022;62:2230–4.
21. Wang L, Shu C, Wang H, Jiao T, Han Y. Effect of assembly unit of expansive agents on the mechanical performance and durability of cement-based materials. Coatings. 2021;11(6):731. doi:10.3390/coatings11060731.
22. Wang L, Yong H, Lu J, Shu C, Wang H. Influence of coarse aggregate type on the mechanical strengths and durability of cement concret. Coatings. 2021;11(9):1036. doi:10.3390/coatings11091036.
23. Suescum-Morales D, Silva RV, Bravo M, Jiménez JR, Fernández-Rodríguez JM, Brito JD. Effect of incorporating municipal solid waste incinerated bottom ash in alkali-activated fly ash concrete subjected to accelerated CO_2 curing. J Clean Prod. 2022;370:133533. doi:10.1016/j.jclepro.2022.133533.
24. Li P, Guo M, Zhang M, Teng L. Leaching process investigation of secondary aluminum dross: the effect of CO_2 on leaching process of salt cake from aluminum remelting process. Metall Mater Trans B. 2012;43:1220–30. doi:10.1007/s11663-012-9678-7.
25. Xie W, Li H, Yang M, He L, Li H. CO_2 capture and utilization with solid waste. J Clean Prod. 2022;3:199–209.
26. Siddique S, Naqi A, Jang J. Influence of water to cement ratio on CO_2 uptake capacity of belite-rich cement upon exposure to carbonation curing. Cem Concr Compos. 2020;111:103616. doi:10.1016/j.cemconcomp.2020.103616.
27. Mostafaeipour A, Bidokhti A, Fakhrzad M, Sadegheih A, Mehrjerdi Y. A new model for the use of renewable electricity to reduce carbon dioxide emissions. Energy. 2022;238:121602. doi:10.1016/j.energy.2021.121602.
28. Lippiatt N, Ling TC, Pan SY. Towards carbon-neutral construction materials: carbonation of cement-based materials and the future perspective. J Build Eng. 2020;28:101062. doi:10.1016/j.jobe.2019.101062.
29. Xian X, Zhang D, Lin H, Shao Y. Ambient pressure carbonation curing of reinforced concrete for CO2 utilization and corrosion resistance. J CO_2 Util. 2022;56:101861. doi:10.1016/j.jcou.2021.101861.

30. Tang W, Zhan B, Wu C, Kou S. Experimental investigation and mathematical modelling of the carbon dioxide sequestration of cement pastes during pressurized CO_2 curing. Constr Build Mater. 2021;302:124383. doi:10.1016/j.conbuildmat.2021.124383.
31. AL-Ameeri A, ImranRafiq M, Tsioulou O, Rybdylova O. Impact of climate change on the carbonation in concrete due to carbon dioxide ingress: experimental investigation and modelling. J Build Eng. 2021;44:102594. doi:10.1016/j.jobe.2021.102594.
32. GB/T 50080-2016. Standard for test method of performance on ordinary fresh concrete. Beijing, China: General Administration of Quality Supervision, Inspection and Quarantine of the People's Republic of China; 2016.
33. GB/T 7124-2008. Adhesives-determination of tensile lap-shear strength of rigid-to-rigid bonded assemblies. Beijing, China: General Administration of Quality Supervision, Inspection and Quarantine of the People's Republic of China; 2008.
34. GB/T 2794-2022. Determination for viscosity of adhesives. Beijing, China: Standardization Administration of China; 2022.
35. GB/T 17671-2005. Method of testing cements—determination of strength. Beijing, China: The State Bureau of Quality and Technical Supervision Contents; 2005.
36. GB/T 50082-2009. Ministry of housing and urban rural development of the people's republic of China. Beijing, China: Standard for test methods of long-term performance and durability of ordinary concrete; 2009.
37. Peng Y, Meng X, Song F, Xu G. Experimental study on the corrosion characteristics of concrete exposed to acid water containing aggressive carbon dioxide and sodium sulfate. Constr Build Mater. 2022;321:126397. doi:10.1016/j.conbuildmat.2022.126397.
38. Kamal N, Itam Z, Sivaganese Y, Beddu S. Carbon dioxide sequestration in concrete and its effects on concrete compressive strength. Mater Today: Proc. 2020;31:A18–21.
39. Qin L, Gao X, Chen T. Influence of mineral admixtures on carbonation curing of cement paste. Constr Build Mater. 2019;212:653–62. doi:10.1016/j.conbuildmat.2019.04.033.
40. Cao H, Liang Z, Peng X, Cai X, Wang K, Wang H, et al. Research of carbon dioxide curing on the properties of reactive powder concrete with assembly unit of sulphoaluminate cement and ordinary portland cement. Coatings. 2022;12:209. doi:10.3390/coatings12020209.
41. El-Hassan H, Shao Y. Early carbonation curing of concrete masonry units with Portland limestone cement. Cem Concr Compos. 2015;62(4):168–77. doi:10.1016/j.cemconcomp.2015.07.004.
42. Huijgen W, Witkamp G, Comans R. Mechanisms of aqueous wollastonite carbonation as a possible CO_2 sequestration process. Chem Eng Sci. 2006;61:4242–51. doi:10.1016/j.ces.2006.01.048.
43. Zhang D, Shao Y. Effect of early carbonation curing on chloride penetration and weathering carbonation in concrete. Constr Build Mater. 2016;123(4):516–26. doi:10.1016/j.conbuildmat.2016.07.041.
44. Ng A, Hock RL, Yew CW. Strength of concrete with recycled manganese slag. Mater Sci Forum. 2021;1030:88–93. doi:10.4028/www.scientific.net/MSF.1030.88.
45. Huang G, Wang H, Shi F. Coupling effect of salt freeze-thaw cycles and carbonation on the mechanical performance of quick hardening sulphoaluminate cement-based reactive powder concrete with basalt fibers. Coatings. 2021;11(9):1142. doi:10.3390/coatings11091142.
46. Witoon T, Lapkeatseree V, Numpilai T, Cheng C, Limtrakul J. CO_2 hydrogenation to light olefins over mixed Fe-Co-K-Al oxides catalysts prepared via precipitation and reduction methods. Chem Eng J. 2022;428(15):131389. doi:10.1016/j.cej.2021.131389.
47. Alomayri T, Adesina A, Das S. Influence of amorphous raw rice husk ash as precursor and curing condition on the performance of alkali activated concrete. Case Stud Constr Mater. 2021;15(4):e00777. doi:10.1016/j.cscm.2021.e00777.
48. Adesina A. Recent advances in the concrete industry to reduce its carbon dioxide emissions. Environ Chall. 2020;1(3):100004. doi:10.1016/j.envc.2020.100004.